Journal of
Synchrotron
Radiation

ISSN 1600-5775

Received 3 December 2013
Accepted 26 March 2014

The multi-purpose hard X-ray beamline BL10 at the DELTA storage ring

D. Lützenkirchen-Hecht,[a]* R. Wagner,[a] S. Szillat,[a]‡ A. K. Hüsecken,[b] K. Istomin,[b] U. Pietsch[b] and Ronald Frahm[a]

[a]Fachbereich C – Physik, Bergische Universität Wuppertal, Gauss-Strasse 20, D-42097 Wuppertal, Germany, and [b]Department of Physics, University of Siegen, Walter-Flex-Strasse 3, D-57072 Siegen, Germany. *E-mail: dirklh@uni-wuppertal.de

The layout and the characteristics of the hard X-ray beamline BL10 at the superconducting asymmetric wiggler at the 1.5 GeV Dortmund Electron Accelerator DELTA are described. This beamline is equipped with a Si(111) channel-cut monochromator and is dedicated to X-ray studies in the spectral range from ∼4 keV to ∼16 keV photon energy. There are two different endstations available. While X-ray absorption studies in different detection modes (transmission, fluorescence, reflectivity) can be performed on a designated table, a six-axis kappa diffractometer is installed for X-ray scattering and reflectivity experiments. Different detector set-ups are integrated into the beamline control software, *i.e.* gas-filled ionization chambers, different photodiodes, as well as a Pilatus 2D-detector are permanently available. The performance of the beamline is illustrated by high-quality X-ray absorption spectra from several reference compounds. First applications include temperature-dependent EXAFS experiments from liquid-nitrogen temperature in a bath cryostat up to ∼660 K by using a dedicated furnace. Besides transmission measurements, fluorescence detection for dilute sample systems as well as surface-sensitive reflection-mode experiments are presented.

Keywords: X-ray absorption spectroscopy; EXAFS; XANES; X-ray reflectivity; diffraction.

1. Introduction

Synchrotron-based hard X-ray probes are widely used for structure-related studies in materials science, physics, chemistry and biology, and there is an increasing demand especially for X-ray absorption spectroscopic experiments, where the energy dependence of the absorption coefficient is measured in the vicinity and above an absorption edge of an element of interest. In order to increase X-ray-related research activities and to meet the user needs for high-energy photons, a new hard X-ray beamline was installed at the DELTA storage ring of the University of Dortmund, Germany (Tolan *et al.*, 2003). The storage ring usually operates at an electron energy of 1.5 GeV, injection currents of 120 mA and about 10–14 h of lifetime. The new beamline is designed for X-ray absorption spectroscopy, diffraction measurements and surface-sensitive X-ray reflectivity experiments in the energy range between ∼4 keV and 16 keV (∼3.1–0.7 Å) making use of the intense radiation emitted by a superconducting wiggler. There are already two hard X-ray beamlines installed at this wiggler (see Paulus *et al.*, 2005; Krywka *et al.*, 2006, 2007; Lützenkirchen-Hecht *et al.*, 2009), but the broad radiation fan covering about ±13 mrad horizontal beam divergence allowed the installation of a third beamline at this insertion device. In the following, we describe the optical layout and the performance of the beamline including first measurements making use of the experimental possibilities provided there.

‡ Present address: Bruker ASC, Waltherstrasse 49-51, 51069 Köln, Germany.

2. X-ray source and beamline

2.1. X-ray source and front-end layout

The X-ray source for the present beamline is a superconducting liquid-helium-cooled wiggler with 20 poles with a magnetic gap of 18 mm that is usually operated in an asymmetric mode with a magnetic field of 5.3 T in five periods, resulting in a wiggler parameter of 149 and a critical energy of about 8 keV. However, there is also a symmetric mode with different properties available (see Table 1; further details of the wiggler including its emission characteristics are available at http://www.delta.tu-dortmund.de/cms/de/Beschleuniger/Anlage/Speicherring/SAW/index.html). The horizontal divergence of the beam amounts to ±25 mrad in the asymmetric wiggler mode, allowing the parallel operation of three beamlines, *i.e.* beamline 9 (Paulus *et al.*, 2005; Krywka *et al.*, 2006, 2007) in the horizontal center of the wiggler fan, and beamline 8 (Lützenkirchen-Hecht *et al.*, 2009) and the newly installed beamline 10 aligned ±15 mrad to either side. Each of these beamlines utilizes a radiation fan of 3 mrad × 0.7 mrad (horizontal × vertical) as defined by a fixed water-cooled absorber mask ∼12 m from the center of the source. The close installation of the three beamlines and the requirement for well separated optical and experimental hutches results in extremely limited space for all the beamline instrumentation, especially in the region of the front-end and the first optical hutches. A schematic representation of the beamline layout is given in Fig. 1, and the most important specifications of the wiggler source and the beamline are summarized in

Table 1
Specifications of the wiggler source at the DELTA storage ring and beamline 10.

DELTA storage ring current	Typically 120 mA injection current, 10–14 h lifetime	
BL10 source	Superconducting wiggler	
	Symmetric mode	Asymmetric mode
Magnetic field	2.79 T	5.3 T
Magnetic period	14.4 cm	28.8 cm
Magnetic gap	18 mm	18 mm
Number of poles	20 (10 periods)	10 (5 periods)
Wiggler k-parameter	36	149
Radiation power	0.84 W mrad^{-2} mA^{-1}	1.59 W mrad^{-2} mA^{-1}
Critical energy E_c	4.18 keV	7.93 keV
Source flux at E_c (calculated)	3.4×10^{11} s^{-1} mA^{-1} mrad^{-1} (0.1% bandwidth)$^{-1}$	1.1×10^{11} s^{-1} mA^{-1} mrad^{-1} (0.1% bandwidth)$^{-1}$
Source size (v × h)	80 µm × 360 µm	80 µm × 360 µm
Source divergence (v × h)	±0.34 mrad × ±13 mrad	±0.34 mrad × ±25 mrad
Absorber mask	13.0 m from source	
Front-end slits (tilt absorber)	23.8 m from source	
Si (111) monochromator	30.0 m from source	
EXAFS endstation	30.8 m from source	
Diffractometer endstation	31.7 m from source	
Flux at sample position (measured)		~3×10^7 mA^{-1} s^{-1} mm^{-2} (0.017% bandwidth)$^{-1}$ at 8 keV
Beam size at the sample		Typically 1 mm × 6 mm (v × h)

Table 1. It should be mentioned here that a rather simple X-ray optic layout has to be used because of the restrictions dictated by the limited space. In particular, the installation of X-ray mirrors for focusing, suppression of higher harmonics and for a reduction of the heat load on the monochromator was not possible at BL10.

The front-end of the beamline, consisting of the photon absorber, a fast vacuum protection shutter, a fixed absorber mask and the white beam shutter, is located inside the concrete shielding that surrounds the storage ring. The first optics hutch, which is shared with beamlines 8 and 9, contains the tilt absorber at a distance of 23.8 m from the source. This device is used for the definition of the vertical beam size impinging on the Si(111) monochromator (30 m from the source). By changing the tilt angle, the vertical beam size can be adjusted to values of up to 3 mm. In order to obtain a high energy resolution for X-ray absorption spectroscopy, however, a typical setting amounts to only 0.3–1 mm depending on the actual energy. Owing to the limited space available, a white-beam slit system could not be installed at BL10. Therefore the horizontal aperture of the tilt absorber is fixed to 15 mm, which results in a horizontal beam size of 19 mm at the position of the first reflecting plane of the monochromator crystal (see Fig. 1*d*). This size is well adapted to the width of the optical surfaces of the channel-cut crystal of 25 mm.

A water-cooled Be window with a large aperture (70 mm height, 40 mm width) terminates the storage-ring vacuum section in front of the monochromator. Its use is mandatory for the protection of the DELTA ring vacuum, and it has to withstand a pressure difference of 1 bar, so that a thickness of 750 µm was used to ensure mechanical stability. This thickness, however, substantially influences the flux available at lower photon energies $E < 6000$ eV with a transmission of about 55% at 5000 eV only. Thus, the installation of

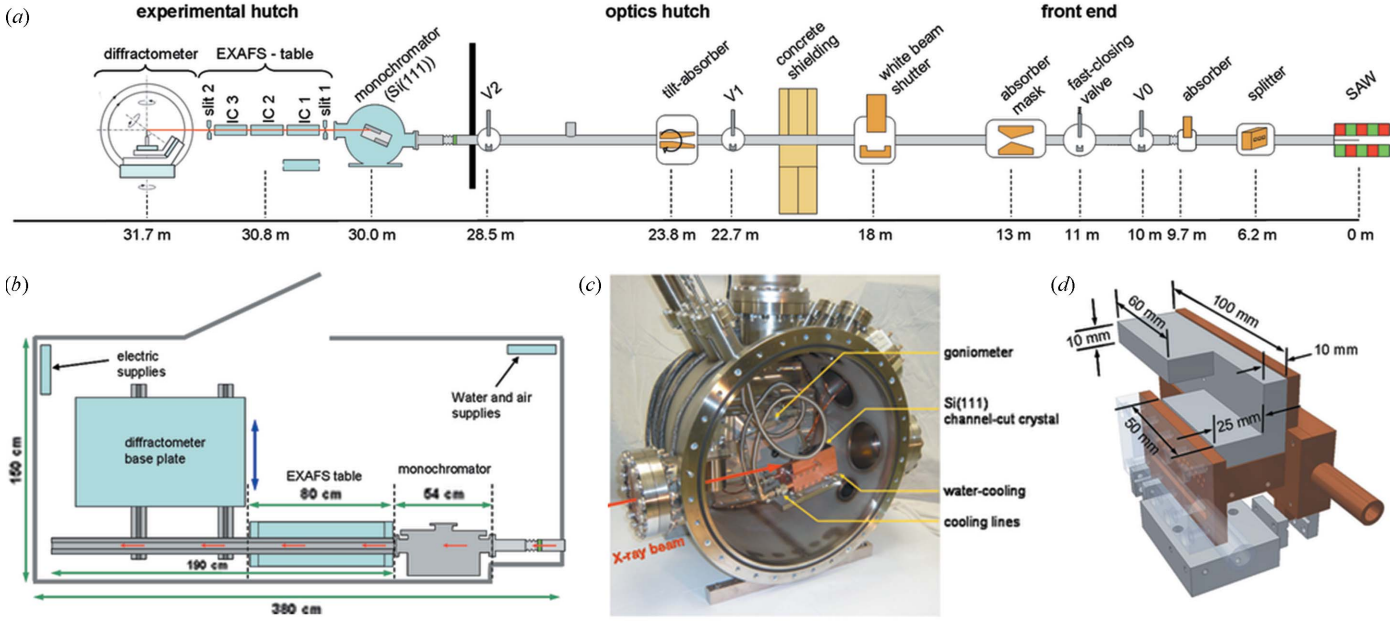

Figure 1
Schematic representation of the basic beamline concept of the DELTA beamline BL10: (*a*) side view and (*b*) top view. Note that the center of the beamline is only separated by 15 mrad from the neighboring beamline BL9, corresponding to only a distance of 45 cm at the position of the monochromator (*c*). This is the reason why the lead shield of the experimental hutch has a transversal offset of ~13 cm between the monochromator of BL10 and the first mirror chamber of BL9. (*d*) Scheme of the channel-cut Si(111) crystal mounted on the water-cooler.

a thinner Be window with a smaller aperture is planned for the near future.

2.2. Monochromator

The channel-cut monochromator (see Fig. 1*c*) is installed in the experimental hutch at a distance of 30 m from the source. Owing to the angular offset of only 15 mrad between adjacent beamlines, the absolute distance between the two X-ray beams of BL9 and BL10 amounts to only 450 mm from the beam centers, and only 12 mrad (*i.e.* 360 mm) if the outer parts of the radiation fan accepted by the fixed absorber are considered. Thus the monochromator construction of BL10 has to fit in between the two radiation fans, and the longitudinal position of the monochromator has to account for the optical components of beamline 9 as well. Therefore the lead shielding between the two beamlines has a ledge of about 13 cm at about 29.5 m from the source. This offset of the wall replicates the contour of the mirror chamber of BL9 in the first part of the experimental hutch of BL10, and it creates the space required for the BL10 monochromator $\sim$0.5 m further downstream.

Here, the center of the X-ray beam passes at a distance of only 280 mm from the lead shield between the hutches, so that an extremely compact monochromator design is mandatory here. Accordingly, the vacuum vessel of the BL10 monochromator has a diameter of only 480 mm and a lateral extension of 380 mm including the top flange and a window. The space available is too small to accommodate two independent monochromator crystals with the necessary linear motions and actuators, and therefore a channel-cut crystal was used instead [see Fig. 1(*d*) for details of the dimensions]. It was mounted with the massive back-plane and the water cooler away from the radiation fan, *i.e.* away from the adjacent beamline BL9 [see Figs. 1(*c*) and 1(*d*)] in order to allow the positioning of the center of the reflecting surfaces in the X-ray beam.

Owing to the limitations in space, the installation of an angular encoder in the monochromator was not possible. In order to verify the stability, repeatability and the reliability of the device, we have performed successive scans of the Au L_3-edge of an Au metal foil between two N_2- and Ar-filled ionization chambers as detectors for incident and transmitted intensities. Between the measurements of those near-edge energy spectra, large energy scans over several keV have been performed, so that the precision of the monochromator can be judged from the accuracy of the resulting edge positions. In Fig. 2, a typical Au spectrum obtained is presented together with a derivative spectrum and the edge positions determined from successive scans by the first maximum of the measured spectra. As can be seen, the edge positions of the spectra differ by significantly less than 0.1 eV from spectrum to spectrum, with a mean value of 11919.22 $\pm$ 0.02 eV as indicated by the dashed lines in the inset of Fig. 2. The difference between the largest and the smallest values measured amounts to 0.06 eV only, thus the energy scale of the present set-up can be considered as stable for spectroscopic investigations with high resolution.

Owing to the fact that rocking-curve measurements are not possible with a channel-cut monochromator, we have measured transmission-mode spectra of several reference metal foils in transmission, and evaluated the width of the derivative spectra (see inset of Fig. 2). Results are compiled in Fig. 3, together with the intrinsic energy resolution of Si(111) as resulting from the Darwin theory, *i.e.* $\Delta E = 1.33 \times 10^{-4} E$, and with calculated values for the natural width of the absorption edges according to Krause & Oliver (1979). In general, the deviation between the measured line-width and the values predicted by Krause & Oliver are very small; only for Cr and

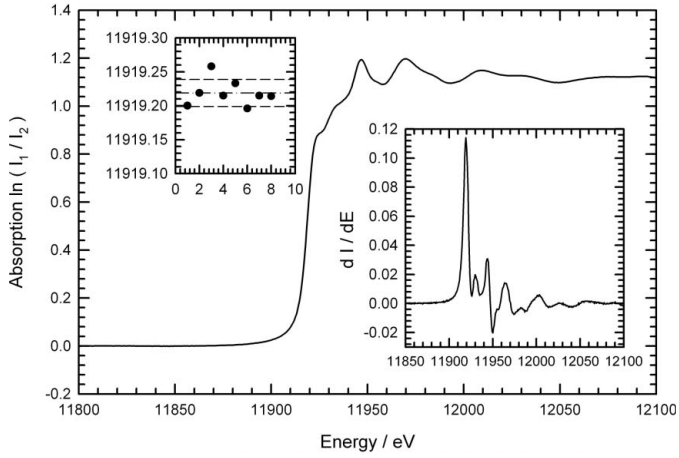

Figure 2
Precision, accuracy and repeatability of the BL10 channel-cut monochromator as determined from repeated measurements of the Au L_3-edge of a gold metal foil. In the insets, a derivative spectrum and the determined edge positions are presented.

Zn is a substantially smaller value predicted by the theory. However, the largest difference found amounts to less than 1 eV, and thus the resolution of the monochromator appears to be suited for the measurement of high-resolution XANES data.

The absence of mirrors in the beam in front of the monochromator implicates that the full heat load from the wiggler impinges on the surface of the first crystal, and thus one may argue about thermal distortions of the first monochromator crystal surface. Therefore, three-dimensional finite-element-analysis (FEA) calculations using the *Comsol Multiphysics* software package (version 4.3.2; Comsol Multiphysics GmbH, Göttingen, Germany, http://www.comsol.com) have been performed in order to determine the temperature distribution in the crystal and its thermal deformations. A radiation power of 160 W mrad^{-2} (see Table 1) was used according to an electron current of 100 mA in the DELTA storage ring. At a distance of 30 m to the source, this corresponds to about 0.18 W mm^{-2}, which is considerably less compared, for example, with a bending magnet of the European Synchrotron Radiation Facility (ESRF) or the Advanced Photon Source (APS). The size of the beam was set to 1 mm $\times$ 20 mm (vertical $\times$ horizontal). We have used a temperature

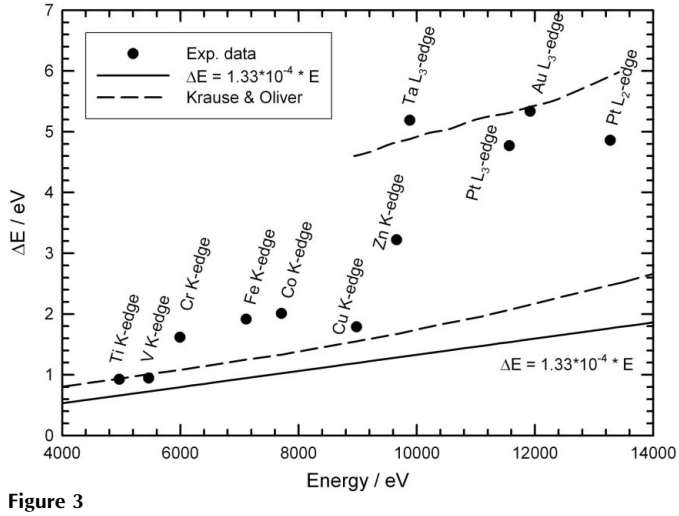

Figure 3
Comparison of experimental values determined for the width of the measured X-ray absorption edges (black circles) as given by the FWHM of the derivative spectra with the Darwin theory (full lines) and the natural line-width values calculated by Krause & Oliver (1979) (dashed lines).

of the cooling water of 293 K and the value for the heat transfer coefficient was set to 5000 W m^{-2} K^{-1} (convective flow). An example of a FEA computation for an incidence angle Θ_B = 20° (corresponding to a photon energy of 5.84 keV) and its evaluation are presented in Fig. 4. Obviously, the surface temperature of the Si crystal increases only slightly to about 298 K in the region where the direct beam from the wiggler hits the crystal, with a small gradient of about 3 K to its back side, where the crystal is mounted onto the water-cooled copper crystal holder. The gradient parallel to the surface varies by about 4 K in about 10 mm distance from the center of the crystal, as can be seen in Fig. 4(*b*), where the temperature distribution along the center of the crystal [dashed white line in Fig. 4(*a*)] is plotted. The resulting deformations of the surface parallel to the surface normal (thermal bump and thermal bowing) are of the order of 1–2 µm only. Depending on the position on the crystal surface, the Bragg angle varies accordingly. In Fig. 4(*c*), these deviations from a plane surface are shown. With values well below ±1 arcsec, the slope errors are significantly smaller compared with the Darwin width of the Si(111) crystal at those energies, and for smaller Bragg angles (*i.e.* higher X-ray energies) the footprint of the beam on the crystal is becoming larger, so that the heat load per surface area decreases and the thermal bump is also reduced. We can therefore conclude that the heat load of the DELTA wiggler only has a negligible influence on the performance of the X-ray monochromator.

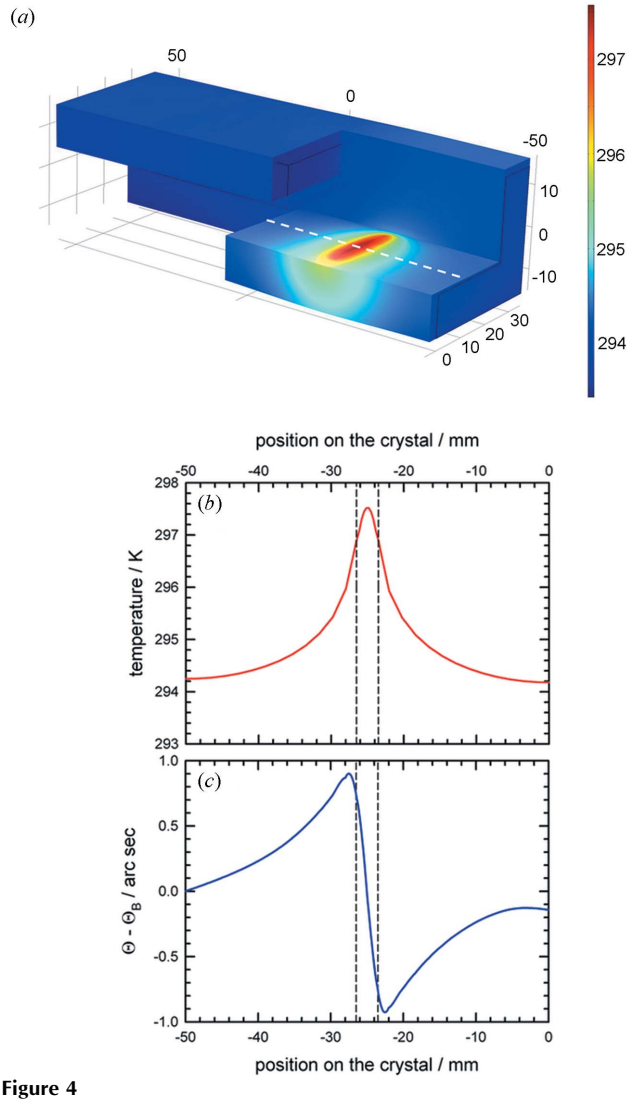

Figure 4
(*a*) Temperature distribution in the indirectly water-cooled channel-cut monochromator crystal as obtained by finite-element analysis (20° Bragg angle, 160 W mrad^{-2}). The obtained temperature along the center of the crystal [dashed white line in Fig. 4(*a*)] is depicted in (*b*), and the resulting slope errors are given in (*c*). The X-ray beam hits the crystal in the region between the dashed vertical lines.

Harmonic rejection is another important issue for any reliable X-ray experiments. One may argue that this is a critical point at BL10 due to the absence of mirrors which act as low-pass filters, and the impossibility to detune the channel-cut monochromator to reduce higher harmonics in the beam. However, owing to the low critical energy of the insertion device, *i.e.* about 4.2 keV in the symmetric mode of the wiggler and 7.9 keV in the asymmetric mode of operation, the intensity of the higher harmonic waves decreases substantially for the photon energy range available at the beamline. Already for the lowest energies around 4 keV the intensity of the third harmonic is reduced by a factor of about eight, and for 8 keV and 10 keV the decrease is even stronger by an order of magnitude and more. Using a proper gas filling of the ionization chambers, this number may be further increased, because the high-energy photons are transmitted by the chambers to a much higher extent. For example, using a 15 cm-long ionization chamber filled with nitrogen gas, the absorption at 5 keV photon energy is about 40%, which decreases to only 2% at 15 keV, *i.e.* by a factor of about 20. At 8 keV, the corresponding numbers are 11.6% and 0.6% for the third harmonic at 24 keV. At 12 keV, assuming an Ar filling of the ionization chamber, the absorption is about 60%, which decreases to ∼3% at the third harmonic at 36 keV. So, in any of the mentioned scenarios, the harmonic suppression adds up to at least 5×10^{-3} or better, which is not as good as in the case of the classical double-mirror set-up, where values of the order of 10^{-4} may be obtained for the harmonic contaminations. Nevertheless, the harmonic suppression achieved at beamline 10 appears to be sufficient for high-quality XANES and EXAFS experiments as detailed below.

Owing to the use of a channel-cut crystal with two flat surfaces, the vertical beam offset Δz of the double-reflected beam changes when the Bragg angle is varied during an energy scan. For a given Bragg angle Θ, Δz may be calculated as $\Delta z = 2D\cos\Theta$, with D being the distance of the Bragg-reflecting surfaces of the channel-cut crystal. Using D = 10 mm, the variation of the vertical beam position during an EXAFS scan of typically 1 keV may be calculated to be about 0.4 mm for a center energy of E = 6 keV, 0.16 mm for E = 8 keV, and well below 0.1 mm for energies above 10 keV. Taking into account that the beam incident on the monochromator typically has a vertical size of about 1 mm, the changing vertical position of the monochromatic beam has no serious influence on the conducted X-ray experiments if the slits downstream of the monochromator are properly aligned. This is especially true for grazing-incidence X-ray experiments, where the vertical size of the beam impinging on the sample is much smaller than that of the white beam upstream of the monochromator. Furthermore, *SPEC* macros are included in the beamline software, that adapt the vertical positions of the EXAFS table and the sample in the diffractometer during an EXAFS energy scan, so that the position of the beam on the sample is maintained.

2.3. Experimental hutch and endstations

With a length of ∼3.8 m and a width of only 1.4–1.5 m (see Fig. 1), the experimental hutch of BL10 is rather small. Keeping in mind that the center of the monochromator is installed about 1.5 m from the lead shielding to the optics hutch, the remaining space of the endstations is less than 2 m. In order to allow a flexible operation

between the different set-ups and making use of the different X-ray techniques, an EXAFS table of about 80 cm length and the six-axis user diffractometer are installed in line directly downstream of the monochromator at about 30.8 m and 31.7 m from the source, respectively. The diffractometer is mounted on rails that allow a translation perpendicular to the beam, so that the entire length of the hutch may be used for EXAFS experiments. On the other hand, an I_0 detector (usually a gas-filled ionization chamber), additional slit systems, beam attenuators and also a He-gas-filled or evacuated flight tube may be mounted on the EXAFS table when the diffractometer is in use.

Ionization chambers with different lengths (15 cm and 30 cm) and different gas supplies (He, N_2, Ar and Kr) are in stock at the beamline as intensity monitors for diffraction, reflectivity and EXAFS experiments. Furthermore, a NaJ-scintillation counter as well as large-area Si pin-diodes and a PIPS detector (passivated implanted planar silicon; Canberra, Meriden, Connecticut, USA) exist with current amplifiers and counter electronics. An additional Peltier-cooled Si drift-diode with digital pulse processing electronics (Amptek, Bedford, USA) is permanently available for X-ray fluorescence and X-ray standing wave (XSW) experiments (see, for example, Zegenhagen, 1993). A first XSW study on paramagnetic Ni–Ti nanoparticles has recently been performed and the results will be published elsewhere (Brücher *et al.*, 2014). In addition, a 2D-area pixel detector (Pilatus 100K; Dectris, Switzerland) is installed on the 2Θ arm of the diffractometer. This detector has already been used for first diffraction experiments (Hüsecken *et al.*, 2013), and X-ray reflectivity measurements are reported below.

Experimental data collection and control of all stepper motors at the beamline is performed by a control software based on the *SPEC* package (Certified Scientific Software, http://www.certif.com). The different devices, motors and also the detectors use different communication hardware and protocols such as VME, GPIB, RS232, USB and TCP/IP. Macros for a variety of scans for diffraction, reflectivity and energy scans, *i.e.* EXAFS, are implemented in the user interface and allow an easy operation and adjustment of the instruments. Furthermore, the digital pulse processors needed for the operation of photon-counting devices, *e.g.* for fluorescence analysis, can also be controlled.

A liquid-nitrogen bath cryostat is permanently available for transmission- and fluorescence-mode EXAFS experiments in the temperature range from room temperature down to about 77 K. Experiments at elevated temperatures may be performed under vacuum or inert gas using a high-temperature cell (Anton Paar domed hot stage DHS 1100 with controller TCU 200) suited for the temperature range from room temperature to 1400 K. This cell features a hemispherical graphite dome and a large-area heater for samples of up to 25 mm diameter. The samples may be directly clamped to the heater enabling X-ray diffraction and EXAFS experiments in reflection geometry, and also grazing-incidence experiments are feasible. Furthermore, using an appropriate sample holder, transmission-mode EXAFS and diffraction studies at elevated temperatures are possible (see below). Both set-ups are permanently available at the beamline and can be installed either on the EXAFS table or on the goniometer of the diffractometer.

The six-axis kappa-type diffractometer (manufactured by Huber Diffraktionstechnik, Rimsting, Germany, http://www.xhuber.de/en/) is mounted at the downstream end of the beamline. All rotations can be performed without any angular limitations with a resolution of 0.001°. Diffractograms of a quartz reference sample in a glass capillary using a scintillation detector or the Pilatus area detector gave sharp diffraction peaks with a typical full width at half-maximum of about 0.1° over the entire angular range. The sample stage of this diffractometer is, however, only suited to small samples, *e.g.* powders, capillary tubes, thin films, *etc.*, but it cannot accommodate heavier equipment like high-temperature cells, ovens, vacuum chambers, *etc*. For this purpose, the kappa circle can be rotated out of the beam, and an additional arrangement composed of a separate cradle with a vertical alignment stage can be attached to the Θ-rotation of the diffractometer. This stage may handle weights of up to about 10 kg, and thus X-ray diffraction, X-ray reflectivity and all kinds of grazing-incidence X-ray studies can be performed employing the equipment required for *in situ* experiments, such as, for example, the high-temperature cell or the cryostat mentioned above.

3. XAFS experiments

3.1. Transmission-mode XAFS experiments

In the commissioning phase of the beamline, several different metal foils have been measured in transmission mode as references (see also Figs. 2 and 3). Fig. 5 summarizes data collected at the L_3-edges of Ta, Pt and Au, using N_2- and Ar-filled ionization chambers for the incident and transmitted intensities, respectively. The spectra were measured at room temperature, each within ∼35–40 min of total acquisition time. In general, the obtained data quality is excellent with respect to the reproduction of sharp absorption features close to the edges as well as to the low noise of the k^3-weighted $\chi(k)$ data. For all elements depicted, almost noise-free data are detected up to wavenumbers close to 20 Å^{-1}, *i.e.* more than 1300 eV above the edges. In the case of Ta and Pt, the measured k-range is only limited by the onset of the L_2-absorption edges at 11136 eV and 13273 eV, respectively. Thus the beamline can be used for high-resolution XANES spectroscopy as well as for the application of the extended X-ray absorption spectroscopy technique in the spectral range between approximately 4 keV and 16 keV. It should be mentioned here that all of the X-ray absorption spectra presented in this communication were collected in the conventional step-scan mode, resulting in acquisition times usually of several minutes. However, the quick-scanning EXAFS (QEXAFS) method is also implemented in the beamline control software. QEXAFS eliminates overheads associated with the movements of the monochromator using a point-by-point scheme by scanning the spectrum continuously. Thus spectra measured on-the-fly are possible within a few seconds (Frahm, 1989). It is worth noting that a channel-cut monochromator in particular appears promising for the realisation of the QEXAFS method owing to its intrinsic mechanical stability and the perfect alignment of the two reflecting monochromator surfaces.

As a first application at BL10, temperature-dependent EXAFS measurements of a polycrystalline zinc foil were performed in order to study in detail the asymmetry of the Zn pair distribution function (Crozier & Seary, 1980; Barrett *et al.*, 1988; Dalba *et al.*, 1999; van Hung *et al.*, 2008; Karolewski *et al.*, 2013). Between liquid-nitrogen (77 K) and room temperature, the measurements were performed in the bath cryostat, while the domed hot stage (see above) was installed for temperatures up to 660 K, *i.e.* close to the melting point of Zn of 692 K. Typical experimental results are shown in Fig. 6, where the Zn K-edge spectrum at 77 K is displayed together with the extracted and k^3-weighted EXAFS function for some selected temperatures. The dramatic decrease of the EXAFS amplitude with temperature can easily be followed. Again, a good data quality was achieved. Even for the spectrum measured at 600 K, almost noise-free EXAFS oscillations are visible up to 15 Å^{-1}. A more detailed analysis of the

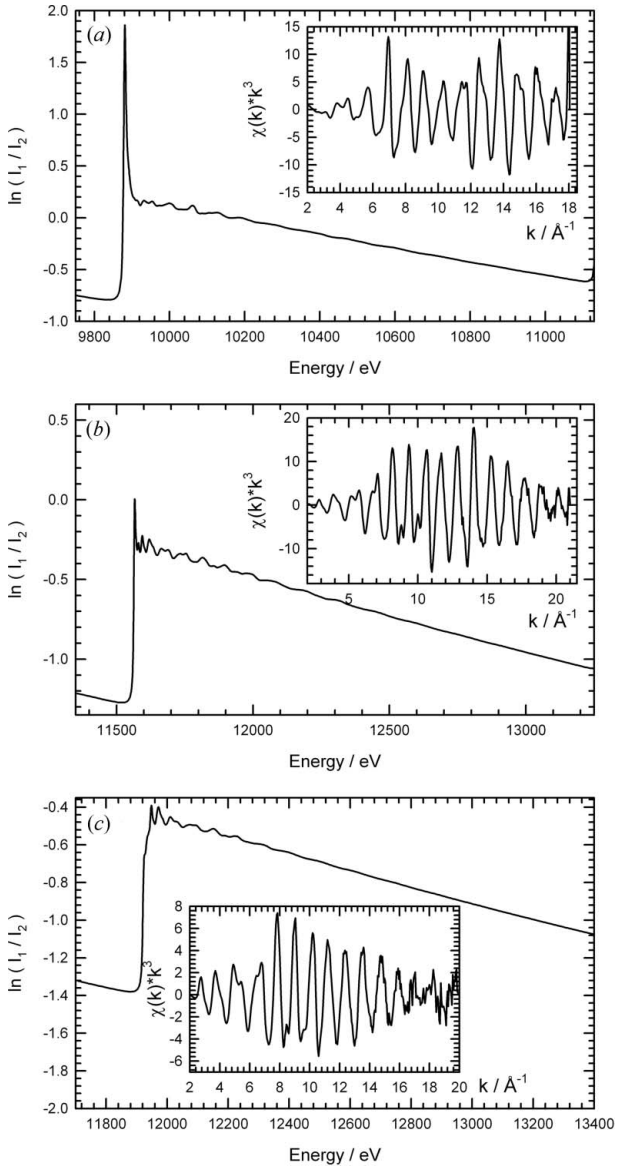

Figure 5
L_3-edge X-ray absorption spectra of Ta (*a*), Pt (*b*) and Au (*c*) metal foils measured in transmission. In the insets the k^3-weighted fine-structure oscillations $\chi(k)k^3$ are depicted.

temperature dependence of the pair-distribution function and its asymmetry is currently under way and will be published elsewhere.

3.2. Fluorescence-mode XANES investigations

For samples that cannot be penetrated by the X-rays or dilute specimens with small absorber concentration, fluorescence-mode XAFS experiments are a useful alternative. Here we have investigated a dilute solution of chloro(triphenylphosphine)gold [$(C_6H_5)_3PAuCl$, CAS No. 14243–64-2] in dichloromethane (CH_2Cl_2). This gold(I) complex has a linear coordination geometry (see Baenziger *et al.*, 1976) and was used as a test sample for fluorescence-mode XANES experiments at the Au L_3-edge. We have prepared a solution by addition of 10 mg of $(C_6H_5)_3PAuCl$ powder with a molar weight of 494.71 g mol^{-1} to 2 ml dichloromethane to obtain a 10 mM l^{-1} concentration of the final solution. The spectra were collected using the large-area PIPS detector (55 mm diameter), and

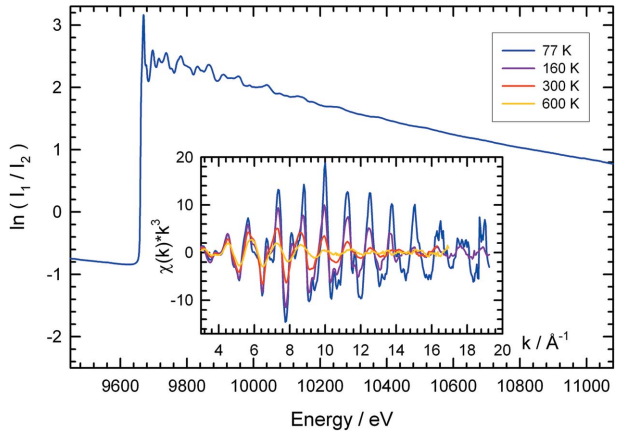

Figure 6
Transmission-mode X-ray absorption spectrum of a polycrystalline zinc foil at the Zn *K*-edge at liquid-nitrogen temperature (77 K). The inset depicts the temperature dependence of the k^3-weighted EXAFS function $\chi(k)$ of the polycrystalline Zn foil.

the fluorescence-mode near-edge spectrum of the Au complex in solution is compared with that of a polycrystalline $(C_6H_5)_3PAuCl$ powder sample measured in transmission in Fig. 7. As can be seen, the XANES features of the solid compound at about 11929 eV, 11948 eV and 11976 eV, labelled A, B and C, respectively, are also present in the spectrum of the dilute $(C_6H_5)_3PAuCl$ solution in dichloromethane, suggesting that the linear structure of the molecule is maintained in the solution.

3.3. Reflection-mode XAFS experiments

Reflection-mode grazing-incidence X-ray absorption spectroscopy is an excellent method for studying the near-surface structure of thin films, surfaces, adsorbates, *etc.* (see, for example, Heald *et al.*, 1988; Borthen & Strehblow, 1995; Jiang & Crozier, 1998; d'Acapito *et al.*, 2002; Lützenkirchen-Hecht *et al.*, 2003). It has intensively been used in the past for the study of oxide layers on metals and alloys, owing to its capability to investigate the structure and the valence of dis-

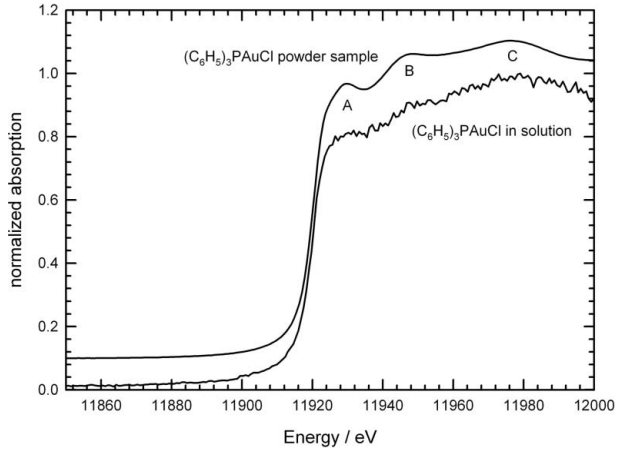

Figure 7
Comparison of the Au L_3-edge XANES spectra of two chloro(triphenylphosphine)gold [$(C_6H_5)_3PAuCl$] samples. While the spectrum of a polycrystalline powder sample was measured in transmission mode using ionization chambers, the spectrum of the dilute liquid sample with a concentration of 10 mM l^{-1} in dichloromethane (CH_2Cl_2) was collected by a PIPS detector in fluorescence mode. The normalized spectra are vertically shifted with respect to each other. The shown spectrum of the Au complex in solution was measured within 25 min of acquisition time.

ordered oxide materials as well (Martens & Rabe, 1981; Barrett *et al.*, 1989; Hüppauff & Lengeler, 1993; Lützenkirchen-Hecht & Strehblow, 2009). Here we want to study the surface oxidation of steels before and after heat treatments in different reactive atmospheres and at elevated temperatures. For the measurements, circular-shaped specimens of diameter 35 mm were polished and mounted on the diffractometer stage. The incident beam was formed by a vertical slit of 0.15 mm and a 7 mm horizontal opening. Incident and reflected intensities were measured using N_2-filled ionization chambers.

In Fig. 8(*a*), spectra obtained at the Fe *K*-edge of the iron-based steel 1.4301 (nominal composition 19.5% Cr, 9% Ni, 1.98% Mn, traces of elements such as Si, Cu, C, P, S, Ti, Mo, V well below 1% and the main contribution of about 65% Fe) are presented for two different incidence angles. For these conditions, the X-ray penetration depth amounts to about 3–4 nm for $\varphi = 0.1^\circ$ and 5–6 nm for $\varphi = 0.25^\circ$ as calculated from the real and imaginary parts of the energy-dependent index of refraction $n(E) = 1 - \delta(E) - i\beta(E)$ (see, for example, Parratt, 1954). As can be seen from Fig. 8(*a*), spectra of reasonable data quality can be measured, and the extracted reflectivity fine-structure oscillations $\Delta R(k)k^2$ appear to have a sufficient signal-to-noise ratio up to at least 10 Å^{-1}. A comparison with the EXAFS of reference compounds (metallic iron, Fe_2O_3, Fe_3O_4) shows that the signals mainly resemble those of Fe, with, however, some smaller contributions from iron oxide. Furthermore, the $\Delta R(k)k^2$ signals change with incident angle with regard to their amplitude and phase. Such a behavior can be expected if a thin oxide layer is present on the steel. If the incidence angle is increased, the penetration depth also increases and the contributions of the underlying metal to the measured X-ray absorption fine structure are increasing, while those of the oxide decrease (see Barrett *et al.*, 1989). Since the X-ray penetration depth amounts to only 3–4 nm for the smaller incidence angle, for which detectable contributions of both metal and oxide are found, it can be deduced that the thickness of the oxide is of a similar size.

In Fig. 8(*b*), a spectrum obtained at the Cr *K*-edge for an incidence angle $\varphi = 0.25^\circ$ is presented. The features in this spectrum resemble that of Cr oxide, suggesting that the air-formed passive film on the steel also includes substantial contributions of Cr_2O_3, as somehow expected (Stypula & Stoch, 1994). In addition to the main constituents of the steel, *i.e.* iron and chromium, it should also be noted that a small feature appears in the chromium spectrum at about 6550 eV [see the arrow in Fig. 8(*b*)]. A magnified view of this feature, measured at $\varphi = 0.1^\circ$, is shown in the inset of Fig. 8(*b*). Obviously, the small amount of less than 2 at% Mn in the steel can be detected by reflection-mode EXAFS, and the XANES features measured suggest the presence of a manganese oxide. This Mn is also probably incorporated in the oxide layer.

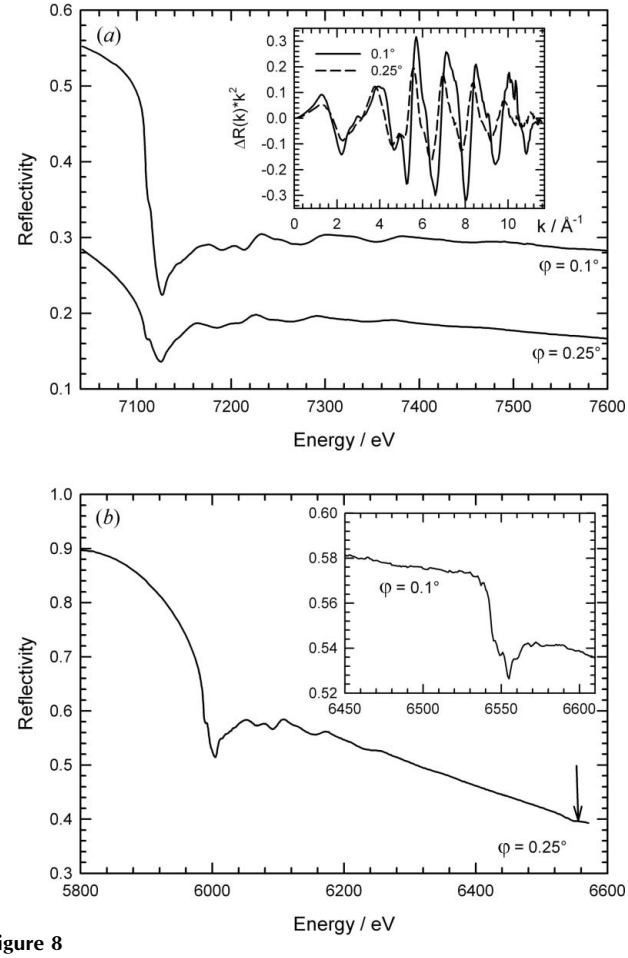

Figure 8
Reflection-mode EXAFS spectra of a steel sample covered with a native oxide layer at different absorption edges: (*a*) Fe *K*-edge for incidence angles $\varphi = 0.1^\circ$ and $\varphi = 0.25^\circ$. In the inset the k^2-weighted reflectivity fine structures $\Delta R(k)k^2$ are shown. (*b*) Cr *K*-edge for an incidence angle $\varphi = 0.25^\circ$. The arrow marks the position of the Mn *K*-edge, which is displayed in the inset for $\varphi = 0.1^\circ$.

4. Conclusions and outlook

The materials science X-ray beamline BL10 at the DELTA storage ring provides a stable X-ray beam for a wide range of investigations and different non-ambient (vacuum, gas and liquid phase, cryogenic and high temperature) environments. The robust Si(111) channel-cut monochromator covers the energy range from about 4 keV up to about 16 keV, giving access to X-ray spectroscopy at the *K*- or *L*-edges of most of the technologically important elements. Besides conventional transmission and fluorescence detection modes, grazing-incidence X-ray absorption spectroscopy as well as X-ray reflectivity and X-ray diffraction experiments are feasible making use of the multi-purpose diffractometer. The results presented in this work demonstrate the good data quality that can be achieved at the beamline. Making use of these opportunities, BL10 has been in user operation since spring 2013, and first scheduled experiments included transmission-, fluorescence- and reflection-mode EXAFS studies. Furthermore, XSW (Brücher *et al.*, 2014) and XRD investigations (Hüsecken *et al.*, 2013) have already been performed.

For the future, detailed tests of the quick-scanning EXAFS capabilities of the beamline are planned. Owing to the high stability and excellent energy resolution offered by the channel-cut monochromator in conjunction with the high photon flux provided by the superconducting wiggler source, time-resolved EXAFS experiments under *in situ* conditions appear feasible, this way allowing real-time investigations of, for example, chemical reactions, catalysts or thin film growth under *in situ* conditions. In conclusion, BL10 represents an attractive instrument for EXAFS studies with hard X-rays. Beam-time proposals can be submitted *via* the DELTA user system at http://usys.delta.uni-dortmund.de, where the beam-time application procedures are described in detail.

This work was financially supported by the MWF NRW. The authors gratefully acknowledge the DELTA machine group for providing reliable synchrotron radiation and for manifold technical support during the installation and the commissioning phase of the beamline. We would like to thank J.-C. Hebig, J. Meyer, T. Nikolova

and D. Wulff for their help with the measurements, and O. Müller for his help with the finite-element calculations.

References

d'Acapito, F., Emelianov, I., Relini, A., Cavatorta, P., Gliozzi, A., Minicozzi, V., Morante, S., Solari, P. L. & Rolandi, R. (2002). *Langmuir*, **18**, 5277–5282.

Baenziger, N. C., Bennett, W. E. & Soborofe, D. M. (1976). *Acta Cryst.* B**32**, 962–963.

Barrett, N. T., Gibson, P. N., Greaves, G. N., Mackle, P., Roberts, K. J. & Sacchi, M. (1989). *J. Phys. D*, **22**, 542–546.

Barrett, N. T., Greaves, G. N., Willis, B. T. M., Antonini, G. M. & Thornley, F. R. (1988). *J. Phys. C*, **21**, L791–L796.

Borthen, P. & Strehblow, H.-H. (1995). *J. Phys. Condens. Matter*, **7**, 3779–3787.

Brücher, M., Chakif, M., Gurevich, E. L., Wagner, R. & Hergenröder, R. (2014). In preparation.

Crozier, E. D. & Seary, A. J. (1980). *Can. J. Phys.* **58**, 1388–1399.

Dalba, G., Fornasini, P., Grisenti, R. & Purans, J. (1999). *J. Synchrotron Rad.* **6**, 253–254.

Frahm, R. (1989). *Rev. Sci. Instrum.* **60**, 2515–2520.

Heald, S. M., Chen, H. & Tranquada, J. M. (1988). *Phys. Rev. B*, **38**, 1016–1026.

Hung, N. V., Tien, T. S., Hung, L. H. & Frahm, R. R. (2008). *Int. J. Mod. Phys. B*, **22**, 5155–5166.

Hüppauff, M. & Lengeler, B. (1993). *J. Electrochem. Soc.* **140**, 598–602.

Hüsecken, A. K., Istomin, K., Wagner, R., Balk, S., Lützenkirchen-Hecht, D., Frahm, R. & Pietsch, U. (2013). *Verh. DPG*, Poster KR5.5.

Jiang, D. T. & Crozier, E. D. (1998). *Can. J. Phys.* **76**, 621–643.

Karolewski, M. A., Cavell, R. G., Gordon, R. A., Glover, C. J., Cheah, M. & Ridgway, M. C. (2013). *J. Synchrotron Rad.* **20**, 555–566.

Krause, M. O. & Oliver, J. H. (1979). *J. Phys. Chem. Ref. Data*, **8**, 329–338.

Krywka, C., Paulus, M., Sternemann, C., Volmer, M., Remhof, A., Nowak, G., Nefedov, A., Pöter, B., Spiegel, M. & Tolan, M. (2006). *J. Synchrotron Rad.* **13**, 8–13.

Krywka, C., Sternemann, C., Paulus, M., Javid, N., Winter, R., Al-Sawalmih, A., Yi, S., Raabe, D. & Tolan, M. (2007). *J. Synchrotron Rad.* **14**, 244–251.

Lützenkirchen-Hecht, D. & Strehblow, H.-H. (2009). *Surf. Interface Anal.* **41**, 820–829.

Lützenkirchen-Hecht, D., Wagemaker, M., Keil, P., van Well, A. A. & Frahm, R. (2003). *Surf. Sci.* **538**, 10–22.

Lützenkirchen-Hecht, D., Wagner, R., Haake, U., Watenphul, A. & Frahm, R. (2009). *J. Synchrotron Rad.* **16**, 264–272.

Martens, G. & Rabe, P. (1981). *J. Phys. C*, **14**, 1523–1534.

Parratt, L. G. (1954). *Phys. Rev.* **95**, 359–369.

Paulus, M., Fendt, R., Sternemann, C., Gutt, C., Hövel, H., Volmer, M., Tolan, M. & Wille, K. (2005). *J. Synchrotron Rad.* **12**, 246–250.

Stypula, B. & Stoch, J. (1994). *Corros. Sci.* **36**, 2159–2167.

Tolan, M., Weis, T., Wille, K. & Westphal, C. (2003). *Synchrotron Radiat. News*, **16**, 9–11.

Zegenhagen, J. (1993). *Surf. Sci. Rep.* **18**, 199–271.